J. Fluid Mech. (2009), *vol.* 638, *pp.* 383–400.
doi:10.1017/S0022112009991224

The origin of oscillations of the large-scale circulation of turbulent Rayleigh–Bénard convection

ERIC BROWN[1]† AND GUENTER AHLERS[2]

[1]The James Franck Institute, University of Chicago, Chicago, IL 60637, USA

[2]Department of Physics and iQCD, University of California, Santa Barbara, CA 93106, USA

(Received 25 February 2009; revised 5 July 2009; accepted 16 July 2009; first published online 1 October 2009)

In agreement with a recent experimental discovery by Xi *et al.* (*Phys. Rev. Lett.*, vol. 102, 2009, paper no. 044503), we also find a sloshing mode in experiments on the large-scale circulation (LSC) of turbulent Rayleigh–Bénard convection in a cylindrical sample of aspect ratio one. The sloshing mode has the same frequency as the torsional oscillation discovered by Funfschilling & Ahlers (*Phys. Rev. Lett.*, vol. 92, 2004, paper no. 1945022004). We show that both modes can be described by an extension of a model developed previously Brown & Ahlers (*Phys. Fluids*, vol. 20, 2008, pp. 105105-1–105105-15; *Phys. Fluids*, vol. 20, 2008, pp. 075101-1–075101-16). The extension consists of permitting a lateral displacement of the LSC circulation plane away from the vertical centreline of the sample as well as a variation of the displacement with height (such displacements had been excluded in the original model). Pressure gradients produced by the sidewall of the container on average centre the plane of the LSC so that it prefers to reach its longest diameter. If the LSC is displaced away from this diameter, the walls provide a restoring force. Turbulent fluctuations drive the LSC away from the central alignment, and combined with the restoring force they lead to oscillations. These oscillations are advected along with the LSC. This model yields the correct wavenumber and phase of the oscillations, as well as estimates of the frequency, amplitude and probability distributions of the displacements.

1. Introduction

Rayleigh–Bénard convection consists of a fluid sample heated from below and cooled from above (for a review, see Ahlers, Grossmann & Lohse 2009). In turbulent convection, a hot (cold) thermal boundary layer at the bottom (top) becomes unstable due to buoyancy and emits hot (cold) volumes of fluid known as 'plumes' which detach from the boundary layer and transport heat vertically. In cylindrical containers with aspect ratio $\Gamma \equiv D/L \approx 1$ (L is the height and D is the diameter of the sample) these plumes contribute to the driving of and are carried by a large-scale circulation (LSC). The LSC on average forms a loop with upflow and downflow on opposite sides of the sample. The dynamics of the LSC include spontaneous diffusive azimuthal meandering of the LSC orientation (Sun, Xi & Xia 2005*a*; Brown & Ahlers 2006*a*,*b*; Xi, Zhou & Xia 2006) and reorientations by both azimuthal *rotations* (Cioni, Ciliberto &

† Email address for correspondence: guenter@physics.uscb.edu

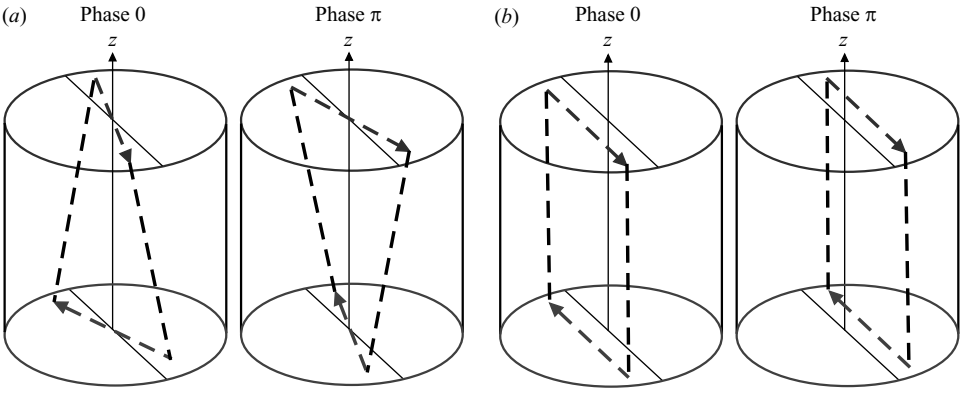

FIGURE 1. (*a*) Diagrams of the twisting oscillation at the extrema. (*b*) Diagrams of the sloshing oscillation at the extrema. The dashed lines represent the LSC and the thin solid lines the references on the vertical z-axis and in the top and bottom planes.

Sommeria 1997; Brown & Ahlers 2006*b*) and *cessations* (Brown, Nikolaenko & Ahlers 2005; Brown & Ahlers 2006*b*). All of these phenomena are now understood on the basis of a simple stochastic model (Brown & Ahlers 2007*a*, 2008*b*) derived from the Navier–Stokes equations by retaining only physically important terms, by taking volume averages that lead to two coupled ordinary differential equations and by adding noise terms to represent the influence of the small-scale turbulent background fluctuations.

It has long been observed that there are temperature and velocity oscillations with frequencies corresponding to the turnover times of the LSC (Heslot, Castaing & Libchaber 1987; Castaing *et al.* 1989; Sano, Wu & Libchaber 1989; Ciliberto, Cioni & Laroche 1996; Takeshita *et al.* 1996; Cioni *et al.* 1997; Qiu & Tong 2000, 2001*a*,*b*, 2002; Niemela *et al.* 2001; Funfschilling & Ahlers 2004; Qiu *et al.* 2004; Sun, Xia & Tong 2005*b*; Tsuji *et al.* 2005; Ahlers, Brown & Nikolaenko 2006). Despite these many measurements the spatial flow structure corresponding to the oscillations remained unclear for a long time. A few years ago an analysis based on shadowgraph images first showed that the spatial structure responsible for the oscillations has a twisting, or torsional, component around the polar axis of the cylindrical container with out-of-phase oscillating azimuthal flows in the top and bottom halves of the sample, as shown in figure 1(*a*) (Funfschilling & Ahlers 2004). The torsional shape was confirmed more recently by temperature measurements along the sidewall (Funfschilling, Brown & Ahlers 2008). Very recently an additional sloshing component of the oscillating structure was discovered by Xi *et al.* (2009) and described in detail by Zhou *et al.* (2009). This mode consists of a time-periodic lateral displacement of the entire LSC circulation plane away from the centreline that is in phase along the entire cylinder axis, as shown in figure 1(*b*).

There have been previous attempts to find the origin of the oscillations. Villermaux (1995) presented a model that attributes the temporal oscillations to periodic emission of thermal plumes from the boundary layers. However, recent experiments showed that there are no periodic correlations between the thermal signals of the top and bottom plates (Xi *et al.* 2009), suggesting that the source of the observed oscillations is to be found in the bulk. Resagk *et al.* (2006) predicted an in-phase torsional-oscillation mode in ellipsoidal containers. The oscillations only existed when the

ellipticity exceeded a critical value; thus this model does not provide a mechanism for any oscillation in cylindrical containers in which the oscillations are usually observed.

The model proposed by us, which describes the spontaneous meandering, rotations and cessations with a pair of physically motivated coupled stochastic ordinary differential equations (Brown & Ahlers 2007*a*, 2008*b*), was extended recently (Brown & Ahlers 2008*a*) with perturbative terms to describe systems with various asymmetries. In one case we predicted an in-phase torsional oscillation in which the restoring force comes from the pressure gradients due to the sidewall in containers with non-circular cross-sections. At the time we did not anticipate the existence of perturbations in which the LSC plane is displaced away from the central cylinder axis, and thus we did not predict the recently characterized sloshing mode. In the present paper we show that the model can be extended to describe the physical mechanism for and the structure of the observed oscillations of the LSC in cylindrical containers by simply relaxing the assumption of a centred LSC circulation plane. We further show that the torsional and sloshing modes can be described simultaneously as a pair of oppositely travelling waves. This behaviour can be predicted by an extension of the model in which we remove the simplifying assumption of a planar (height-independent) LSC and by adding the appropriate advection term.

In the next section we present the results of new analyses of experimental data from Brown & Ahlers (2006*b*, 2008*a*,*b*). First, in § 2.1, we discuss the sinusoidal fitting-function (SF) analysis method used by us previously and the 'temperature-extremum-extraction' (TEE) method introduced by Xi *et al.* (2009). There we also present an extended SF method which includes higher harmonics that enable the detection of the sloshing mode and a measurement of the sloshing amplitude. In that section a comparison of time series for the slosh displacement angle obtained by the extended SF method and the TEE method is presented. In § 2.2 we examine the probability-distribution functions of the slosh displacement and of the torsional displacement. In § 3 we extend the model presented by us previously (Brown & Ahlers 2007*a*, 2008*b*) and show that it can explain the existence of the sloshing mode as a consequence of the restoring force that arises from a lateral displacement of the LSC circulation plane due to the turbulent background fluctuations and away from the sample centreline. In § 4 we show that this model also leads naturally to the torsional oscillation discovered several years ago (Funfschilling & Ahlers 2004); the origin of this mode had been unexplained before because the model had been restricted to an LSC with a circulation plane that contains the vertical sample centreline. Finally, in § 5, we summarize the contents of this paper and discuss the broader applicability of its approach to other geometries.

2. Experimental results for the slosh displacement

2.1. *Analysis methods and the slosh displacement angle*

We use data obtained originally by Brown & Ahlers (2008*b*) to search for the sloshing mode. The results presented here are for a Rayleigh number $Ra \equiv \beta g \Delta T L^3/(\kappa\nu) = 1.1 \times 10^{10}$ and Prandtl number $Pr \equiv \nu/\kappa = 4.38$ (β is the isobaric thermal expansion coefficient, g the acceleration of gravity, ΔT the applied temperature difference, L the sample height, ν the kinematic viscosity and κ the thermal diffusivity). The sample was a water-filled cylinder with $L = 24.76$ cm and aspect ratio $\Gamma \equiv D/L = 1.00$ (D is the sample diameter). The data consisted of temperature measurements by thermistors embedded in the sidewall. There were

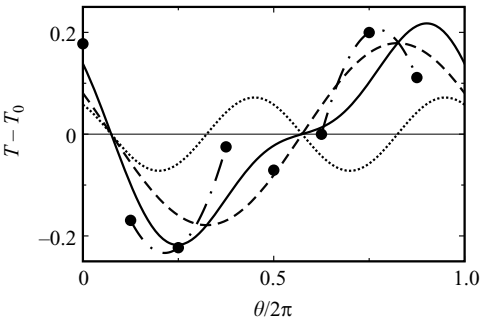

FIGURE 2. Example of a temperature profile measured by the sidewall thermistors at the midplane for $R = 1.1 \times 10^{10}$. The thin dash-dotted lines denote the TEE fit of extrema; the dashed line denotes cosine fit of (2.1); the dotted line denotes second-order sinusoidal term A_2 obtained from fitting (2.2) to the difference between the data and the cosine fit; the thick solid line denotes the fit obtained from the Fourier-moment method, corresponding to the sum of the dashed and dotted lines.

eight thermistors, equally spaced azimuthally, at each of three different heights: the mid-height which is defined to be at $z = 0$, height $z = L/4$ and height $z = -L/4$.

The temperature measurements capture the behaviour of the LSC by detecting the upward, hot flow on one side and downward, cold flow usually on the opposite side of the container. Previously, to characterize the LSC, we fit a sinusoidal function

$$T(\theta) = T_0 + \delta \cos(\theta - \theta_0) \tag{2.1}$$

to the thermistor temperatures measured around the sidewall at a given height (Brown *et al.* 2005; Ahlers *et al.* 2006; Brown & Ahlers 2006*b*; Funfschilling *et al.* 2008). The orientation of the LSC was defined as θ_0, corresponding to the hot side of the sample with upward flow. The amplitude of the LSC is characterized by δ. An example is shown by the dashed line in figure 2. This fitting function was useful for studying azimuthal diffusion and cessations of the LSC, as well as torsional displacements and oscillations in which the maximum and minimum of the temperature profile have a phase separation of π. The sloshing oscillation was discovered and characterized (Xi *et al.* 2009; Zhou *et al.* 2009) using instead the TEE method for obtaining the orientation α_h of the maximum and the orientation α_c of the minimum of the azimuthal temperature profile. The TEE consists of fitting a quadratic function to each of the two temperature extrema and their two neighbouring temperatures, as shown in figure 2 by the two thin dash-dotted lines (each of which passes through three data points). The extremum of the quadratic fit is taken as the orientation. The SF has the advantage of using all the information from the eight temperatures at a given height, but does not allow the phase difference between α_h and α_c to differ from π. Thus it cannot detect the sloshing mode. The TEE uses information from only three thermometers at a time, but does not have the phase constraint and thus can reveal the sloshing mode. We used the TEE method to re-analyse data from earlier experiments (Brown & Ahlers 2006*b*, 2008*a*,*b*) and found that those data also contained information about the sloshing oscillations. We define the angles α_h and α_c with a built-in phase difference of π so that $\alpha_h = \alpha_c$ corresponds to a centred LSC circulation plane and counterclockwise displacements are positive. The slosh displacement angle is then $\alpha' \equiv (\alpha_h - \alpha_c)/2$. An example of a time series of the slosh displacement angle α' obtained with the TEE method is shown as open circles in figure 3. Since the TEE method fits to only three thermistor readings whereas the

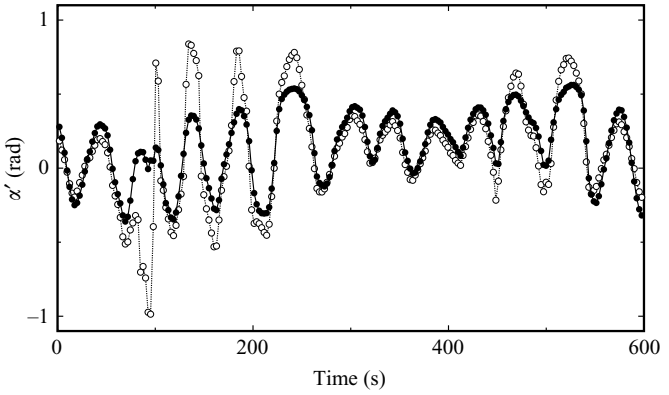

FIGURE 3. Time series of the slosh displacement angle $\alpha' = (\alpha_h - \alpha_c)/2$ for the middle-row thermistors at $R = 1.1 \times 10^{10}$: solid circles, from the Fourier-moment method; open circles, from the TEE method of Zhou *et al.* (2009).

sinusoidal fit uses eight, the TEE method is more susceptible to being biased by local temperature fluctuations when the signal is very noisy. (In a typical case, the root-mean-square noise amplitude due to turbulent fluctuations is approximately 0.28δ at $R = 1.1 \times 10^{10}$; Brown & Ahlers 2007*b*.) An example of this can be seen in figure 2 in which the high temperature at $\theta = 0$ does not contribute to the determination of the extrema even though it is only 11 % below the highest measured temperature, well within the typical fluctuation level; thus it cannot be determined which point better represents the LSC extrema. To better deal with these local fluctuations we developed a method of characterizing the sidewall temperature profile based on Fourier moments. The dominant term was the cosine fitting function (2.1). We took the Fourier series of the difference between that fit and the actual signal. While cosine terms are still symmetric and thus cannot contribute to a slosh displacement, the antisymmetric sine terms can characterize the off-centre displacement as a perturbation of the dominant cosine term. We calculated the sinusoidal Fourier amplitudes

$$A_n = [T - T_0 - \delta \cos(\theta - \theta_0)] \sin[n(\theta - \theta_0)]. \tag{2.2}$$

The $n = 1$ term was found to be zero because all it would do is shift the temperature profile, which had already been taken care of by the fit of θ_0. Higher-order terms showed strong fluctuations, and the power spectra of mode amplitudes corresponding to $n = 2, 3, 4$ are shown in figure 4. These higher-order moments all have the same background, similar to the backgrounds of other power spectra measured in the same system (Funfschilling *et al.* 2008). The $n = 2$ term has a peak in the power spectrum at a frequency of 0.02011 ± 0.00003 Hz, equal to that observed by cross-correlations of thermistors on opposite sides of the sample which was 0.02008 Hz for this $R = 1.1 \times 10^{10}$ (Brown, Funfschilling & Ahlers 2007). This suggests that the cross-correlation also measured the slosh frequency, as suggested originally by Zhou *et al.* (2009). Since the A_2 term is the only one which differs from a noise distribution, the temperature profile can be described by the cosine term plus the $n = 2$ term. For $A_2 \neq 0$, the temperature profile is tilted so that the extrema become closer together, corresponding to a slosh displacement. The slosh displacement angle α' satisfies the equation $\delta \sin \alpha' = 2A_2 \cos(2\alpha')$. An example of this fit is shown in figure 2 in which it also is compared with the other fitting methods. It is seen that this fits the data better than the cosine method by itself. In this example, the TEE method gave a peak to

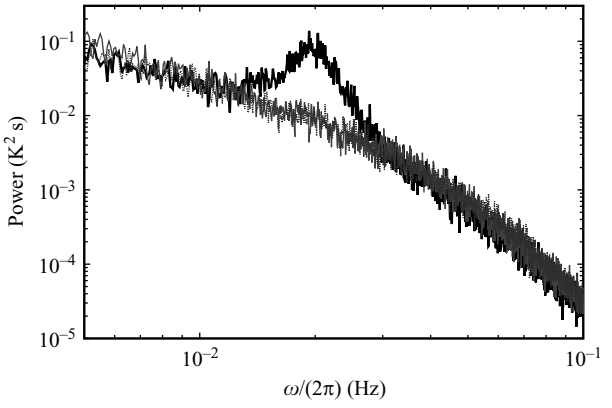

FIGURE 4. The power spectra of the sinusoidal Fourier moments of the temperature profile $T(\theta)$ for the middle-row thermistors at $R = 1.1 \times 10^{10}$. The solid line denotes second-order moment ($n = 2$), the grey line third-order moment ($n = 3$) and the dotted line fourth-order moment ($n = 4$). Although away from the peak it is difficult to distinguish the three, it is clear that they all agree with each other except that only the second moment (solid line) has a pronounced maximum. The power spectra were smoothed for clarity.

the left of that found by the cosine method, while the Fourier-moment method gave a peak to the right. A time series of α' comparing this fitting method with the TEE method is shown in figure 3 as solid circles. From this time series, the oscillations reported by Xi *et al.* (2009) can clearly be seen. As expected, the modified SF is found to be smoother than the TEE method because it makes use of all eight thermistor measurements and so is less susceptible to local fluctuations. All cross-correlation functions between α' measured at any two different heights show oscillations that are in phase with each other, consistent with a sloshing oscillation. Thus our observed oscillations are in agreement with those of Xi *et al.* (2009) and Zhou *et al.* (2009).

2.2. *Probability distributions of the slosh and the torsional displacements*

The probability distributions of α' based on the Fourier-moment method, computed separately at each of the three vertical positions ($z = \pm L/4, 0$) for $R = 1.1 \times 10^{10}$, are shown in figure 5(a). They do not differ very much from each other. They are very flat and even slightly double-peaked, in agreement with the results of Zhou *et al.* (2009). We found that $p(\alpha')$ varied depending on the fitting method used (see § 2.1), which is why we developed the Fourier-moment method to filter out much of the noise and minimize the effect of local fluctuations on α'. We also computed the probability distribution $p(\langle\alpha'\rangle_z)$, where $\langle\alpha'\rangle_z$ is the average of α' over the three levels at any given moment in time. This is given in figure 5(b) as open circles. Although on average the slosh oscillations are in phase at all three heights, the shape of the height-averaged probability distribution changes to a single-peaked distribution that is closer to Gaussian in shape. We attribute this to random fluctuations of the relative phases at the three levels which are largely uncorrelated. A Gaussian fit to the peak gives a width of $\sigma_{\alpha'} = 0.27$ rad. In § 3 we will present a model that yields such a Gaussian $p(\langle\alpha'\rangle)$. We will also present a model that includes the twist oscillation in § 4. A height-averaged twist amplitude can be represented by $[\theta_0(L/4) - \theta_0(-L/4)]/2$. This is plotted in figure 5(b) for the same data set as open squares. A Gaussian fit to the peak gives a width of $\sigma_{\theta'} = 0.18$ rad.

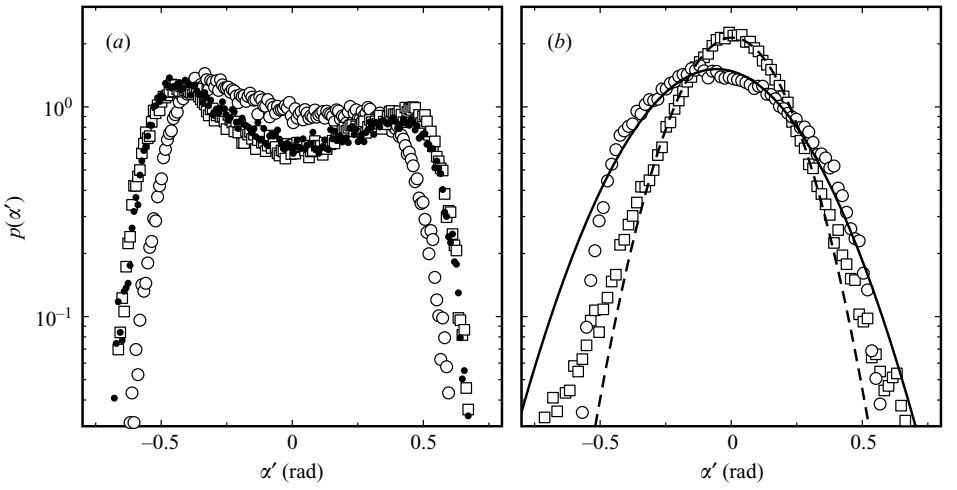

FIGURE 5. Probability distributions of the slosh and torsional displacement angles obtained from the Fourier-moment method at $Ra = 1.1 \times 10^{10}$. (*a*) The slosh mode at $z = L/4$ (top row of thermistors, open squares), $z = 0$ (middle row of thermistors, open circles) and $z = -L/4$ (bottom row of thermistors, solid circles). (*b*) Open circles: probability distribution of the slosh displacement $\langle \alpha' \rangle_z$, where $\langle \alpha' \rangle_z$ is the displacement averaged over the three rows of thermistors at fixed time. Solid line: Gaussian fit to the open circles near the peak. Open squares: the probability distribution of the twist displacement angle $\theta' = [\theta_0(L/4) - \theta_0(-L/4)]/2$. Dashed line: Gaussian fit to the open squares near their peak.

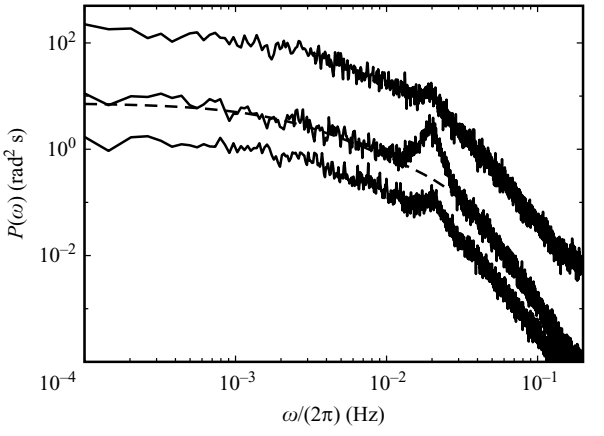

FIGURE 6. The solid lines denotes the power spectra $P(\omega)$ of the slosh amplitude at $Ra = 1.1 \times 10^{10}$ at the three vertical positions. Results for the top (bottom) row of thermistors at $z = L/4$ ($z = -L/4$) were multiplied (divided) by a factor of 10 in order to make all three data sets distinguishable from each other. The dashed line denotes a fit of the predicted power spectrum for the background from (4.9) to the midplane ($z = 0$) data.

2.3. *Power spectra*

Power spectra $P(\omega)$ of α' are shown separately for the three vertical positions in figure 6. Despite the fact that $p(\alpha')$ is narrowest at the midplane, the peak of the power spectrum is larger at the midplane in agreement with Zhou *et al.* (2009), showing that the oscillation amplitude is larger there. Besides showing a peak which gives the oscillation frequency, the measured power spectrum has several distinct

scaling regions. It reaches a constant in the limit of small frequency, scales as ω^{-1} before the peak and scales as ω^{-4} in the large-frequency limit. In § 4 we will present a model power spectrum that fits well to this data.

3. Model for the sloshing oscillation

3.1. *The basic model*

The dynamics of the midplane orientation θ_0 of the LSC in cylindrical containers can be described by a stochastic ordinary differential equation in terms of the measured parameters θ_0 and δ. This equation was obtained by taking approximate volume averages of appropriate terms of the Navier–Stokes equation (Brown & Ahlers 2007*a*, 2008*b*). The full derivation has been given by Brown & Ahlers (2008*b*), but we will describe it briefly here. In the simplest case with no asymmetries, there is nothing to drive the azimuthal dynamics of the LSC other than turbulent fluctuations which are represented by a stochastic term $f_{\dot{\theta}}(t)$. This term could be represented by a Gaussian white noise distribution which can be described by a single parameter: a diffusivity $D_{\dot{\theta}}$ whose value was obtained from experiments (Brown & Ahlers 2008*b*). The damping of the dynamics was found to be dominated not by viscosity but rather by rotational inertia which comes out of the nonlinear advective term of the Navier–Stokes equation. This term is coupled with the flow strength of the LSC which we characterize by the measured temperature amplitude δ. Putting these terms together with the inertial term gives the Langevin equation

$$\ddot{\theta}_0 = -\frac{\delta\dot{\theta}_0}{\delta_0\tau_{\dot{\theta}}} + f_{\dot{\theta}}(t). \tag{3.1}$$

Here δ_0 represents the mean value of δ and $\tau_{\dot{\theta}}$ (=6.9 s for $R = 1.1 \times 10^{10}$) is the inherent damping time scale of the system. The behaviour of the temperature amplitude δ can be described by a separate equation in which δ_0 is determined by a balance between buoyancy and drag forces and in which its dynamics are driven by another stochastic term. The dynamics consist of fluctuations around a stable fixed-point value δ_0, with occasional (about once per day) large fluctuations to an unstable fixed point at $\delta = 0$ corresponding to cessations of the flow. These equations successfully described the azimuthal meandering of the LSC orientation seen in experiments and gave estimates of the measurable physical parameters which were typically good within about a factor of two (Brown & Ahlers 2007*a*). For the purposes of the present work we focus only on azimuthal oscillations which we will obtain by adding a restoring force to (3.1). The cessations are rare (about once per day, compared to an oscillation period of 49 s at $R = 1.1 \times 10^{10}$). Thus they occur independent of the oscillations and the vast majority of the time we can approximate $\delta = \delta_0$ and eliminate the coupling altogether. In this limiting case the dynamics of (3.1) correspond to diffusive fluctuations. In cases in which fluctuations in the damping term can affect the dynamics, they are well described on the time scale of the oscillations as Gaussian distributed with width $0.22\delta_0$ (Brown & Ahlers 2008*b*). This model was extended by Brown & Ahlers (2008*a*) to include perturbations that break the rotational invariance of the original model. In particular, it provided a qualitative explanation for why non-circular cross-sections cause the LSC circulation plane to align along the longest diameter. The predicted mechanism depends on the restoring pressure provided by the sidewall. The primary component of this pressure exists also for the rotationally invariant case and provides the force to drive the LSC in a closed loop. A secondary component appears when

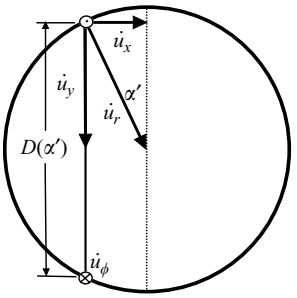

FIGURE 7. A horizontal cross-section showing the sidewall forcing for a horizontal displacement of the LSC. The solid vertical line corresponds to the plane of the LSC when it is displaced from a central alignment by the slosh displacement angle α'. The component $\dot{u}_y$ of the normal force F provides the centripetal acceleration for the LSC, and the component $\dot{u}_x$ acts as the restoring force for a sloshing oscillation. The primary LSC velocity u_ϕ is perpendicular to this cross-section.

the rotational invariance is broken and pushes the LSC towards alignment with the longest diameter. For non-circular cross-sections, the sidewall pressure yields a potential dependent on a diameter function $D(\theta)$ corresponding to the azimuthally varying container diameter for an LSC that always crosses the centre of the container (Brown & Ahlers 2008*a*). This gives a preferred orientation aligned with the longest diameter with possible oscillations driven by stochastic fluctuations.

3.2. *Potential due to pressure forcing from the sidewalls*

Here we show that the same sidewall pressure mechanism can explain the sloshing oscillations of the LSC in containers with circular cross-sections. The result turns out to be determined by a diameter function that depends on the off-centre displacement of the LSC circulation plane. This function is analogous to the case for containers with non-circular cross-sections. We will calculate model terms for containers of height and diameter both equal to L and with circular horizontal cross-sections for comparison with experiments, but this geometrical restriction is not necessary in general. (but of course the geometry has to be such that a single-loop LSC is a good approximation to the physical system). To allow for a slosh displacement we must relax the original assumption that the LSC circulation plane passes through the cell centreline. The diameter as a function of slosh displacement in a cylindrical container is $D(\alpha') = L\cos\alpha'$. For simplicity we consider a planar LSC with an infinitesimal width. We will cover a non-planar LSC in §4. The model can be simply explained based on a vector force balance on the plane of the LSC at the inner edge of the viscous boundary layer at the sidewall at which the vertical velocity peaks. This result can be added as a perturbation to the Langevin equation (3.1). The radial pressure provided by the sidewall can be broken down into two orthogonal components: one along the plane of the LSC which provides the centripetal acceleration $\dot{u}_y = 2u_\phi^2/D(\alpha')$ and one perpendicular to the LSC plane which must then equal $\dot{u}_x = \dot{u}_y \tan\alpha'$. A diagram of this is shown in figure 7. The LSC velocity at the edge of the viscous boundary layer is represented as $u_\phi = \omega_\phi L/2$ so that ω_ϕ and u_ϕ are independent of α', equivalent to the form used by Brown & Ahlers (2008*a*). Combining these terms gives the contribution to angular acceleration from pressure forces,

$$\ddot{\alpha}'_g = \frac{2\dot{u}_x}{D(\alpha')} = -\omega_\phi^2 \frac{\tan\alpha'}{\cos^2\alpha'}. \tag{3.2}$$

The pressure of the sidewall provides a restoring force for the plane of LSC if it is off-centre. While the LSC plane had originally been assumed to be aligned with the cell centre, the off-centre alignment can be generated by the action of turbulent fluctuations. We can describe the dynamics by adding $\ddot{\alpha}'_g$ as a perturbative term to a dynamic equation for α' analogous to (3.1), assuming the stochastic and damping terms are the same for this off-centre perturbation of the LSC as for other modes:

$$\ddot{\alpha}' = -\frac{\delta\dot{\alpha}'}{\delta_0\tau_{\dot{\theta}}} - \omega_\phi^2 \frac{\tan\alpha'}{\cos^2\alpha'} + f_{\dot{\theta}}(t). \tag{3.3}$$

The slosh dynamics can be expressed in terms of diffusion in an azimuthal potential given by

$$V_g \equiv -\int \ddot{\alpha}'_g \, \mathrm{d}\alpha' = \frac{\omega_\phi^2 L^2}{2D(\alpha')^2}, \tag{3.4}$$

where $D(\alpha') = L\cos\alpha'$. This is written in terms of the diameter function with the same form as the effect of the cross-section geometry (Brown & Ahlers 2008*a*). In principle the diameter function could be calculated for slosh displacements in different cross-section geometries. An alternate derivation based on volume-averaging the Navier–Stokes equations throughout the sample was given by Brown & Ahlers (2008*a*) and produces the same result.

We derived equations assuming the width of the LSC is infinitesimal for simplicity. Accounting for a finite width of the LSC is not expected to qualitatively change results; it may have the effect of smoothing out the potential near the minimum, and the potential may increase dramatically at an angle smaller than $\pi/2$ due to the LSC being forced to the side of the container.

3.3. *Oscillations*

We can obtain a linearized Langevin equation from (3.3) by assuming small α' and assuming $\delta = \delta_0$ which is a good approximation in experiments except during cessations. This equation is given by

$$\ddot{\alpha}' = -\frac{\dot{\alpha}'}{\tau_{\dot{\theta}}} - \omega_\phi^2\alpha' + f_{\dot{\theta}}(t). \tag{3.5}$$

The resonant frequency of the deterministic part of the equation is

$$\omega_r = \sqrt{\omega_\phi^2 - 1/\left(4\tau_{\dot{\theta}}^2\right)}. \tag{3.6}$$

This corresponds to the natural frequency ω_ϕ when the damping term is small compared to the restoring term and is of the same order as the frequency of the LSC turnover as observed in experiment (Xi *et al.* 2009). The natural frequency scales with the turnover frequency as observed because the restoring force comes from sidewall pressure which balances with the centripetal acceleration of the LSC.

3.4. *Probability distribution*

The probability distribution of the orientation can be obtained from the steady-state Fokker–Planck equation in the strong-damping limit and is

$$p(\alpha') \propto \exp\left(-\frac{V_g}{\tau_{\dot{\theta}} D_{\dot{\theta}}}\right). \tag{3.7}$$

Expanding V_g up to second order gives a Gaussian distribution with width $\sigma_{\alpha'} = \sqrt{D_{\dot{\theta}}\tau_{\dot{\theta}}}/\omega_\phi$. Based on experimental measurements of the parameters $\tau_{\dot{\theta}}$ and $D_{\dot{\theta}}$

(Brown & Ahlers 2008*b*) we expect $\sigma_{\alpha'} \approx 0.22$ rad at $Ra = 1.1 \times 10^{10}$ and a Rayleigh-number dependence proportional to $Ra^{-0.22}$. The predicted width of the distribution is close to the value 0.27 rad found in § 2.2 with no significant trend with Ra (Zhou *et al.* 2009). Since there are oscillations, a strong-damping solution is not exact but nonetheless gives an estimate for the amplitude.

If we consider the prediction for larger α, we note the restoring force diverges at $\alpha' = \pi/2$, which means that the amplitude of α' is strongly bounded to remain less than $\pi/2$. This is physically significant because at $\alpha' = \pm\pi/2$ the LSC would be confined to a vertical line at the side of the container. The typical amplitude of oscillation is on the same scale, so if the potential did not turn up sharply large fluctuations could lead to a break-up of the LSC. This specific form of break-up has not been observed. The drop-off in the probability distribution shown in figure 5 occurs at a smaller displacement angle of about 0.6 rad, which would be expected due to the finite width of the LSC.

4. The torsional oscillation

The sloshing oscillation occurs along with a torsional oscillation with out-of-phase azimuthal flows in the top and bottom halves of the sample of approximately the same frequency and amplitude (Funfschilling & Ahlers 2004; Funfschilling *et al.* 2008; Zhou *et al.* 2009). These two modes seem to be sufficient to describe all of the observed temperature and velocity oscillations. Even observations that at first suggested different structures can be described as being due to projections of the sloshing oscillation combined with the spontaneous meandering of the LSC. These include out-of-phase anti-correlations between temperatures at opposite sides of the sample (Ahlers *et al.* 2006; Brown *et al.* 2007) and apparent sloshing parallel to the LSC plane (Zhou *et al.* 2009). Thus if we can describe both sloshing and torsional oscillations, we can describe all of the observed oscillatory dynamics. Some measurements indicated a difference of up to 20 % between two observed frequencies measured by different methods depending on Ra (Brown *et al.* 2007), but for now we will consider this as a perturbation and first try to explain why the frequencies should be the same. Both the sloshing and torsional oscillations have been described in the Eulerian frame in which they appear to have a phase difference of $\pi/2$ so that the sloshing oscillation amplitude is maximized while the twist oscillation amplitude is zero and the signal at the midplane follows the bottom row on the hot side but follows the top row on the cold side. It was noted by Zhou *et al.* (2009) that this direction is consistent with the direction of advection through the sample with the LSC. If we instead consider this flow in the meridionally moving Lagrangian frame of the LSC, the motion is simply a horizontal oscillation of the plumes, as they are advected along with the LSC such that the hot and cold plumes are always moving in opposing directions. The oscillation is drawn in both the Eulerian and Lagrangian frames in figure 8. This suggests that the combination of sloshing and torsional oscillations can be reinterpreted as travelling waves consisting of oppositely moving plumes.

We now take the step of writing down the equations for these travelling waves. The nodes of the sloshing oscillation are observed to be at the top and bottom plates, and the antinode is found at the midplane (Zhou *et al.* 2009). The node of the torsional oscillation is observed to be at the midplane (Funfschilling *et al.* 2008). For ease of comparison to sidewall measurements we will assume the path of the LSC to be square around the edge of the sidewall with a length of $4L$. This differs from the assumption of a circular LSC shape in § 3, where we needed to calculate

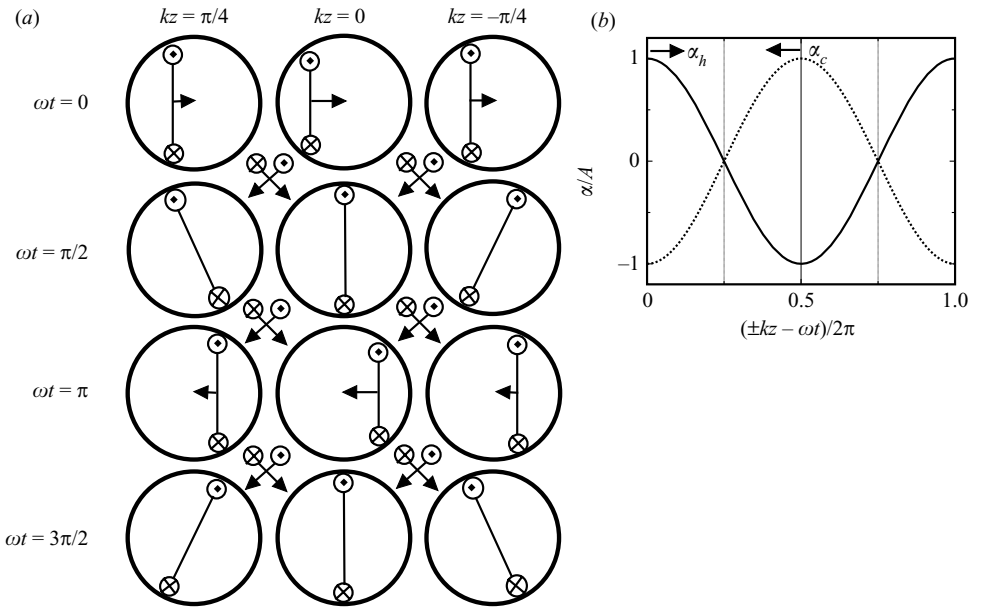

FIGURE 8. (*a*) The torsional and sloshing oscillations at different heights and phases in the Eulerian frame. Circled dot denotes α_h where the LSC flow is upward. Circled cross denotes α_c where the LSC flow is downward. Connecting lines denote the local plane of the LSC. Arrows pointing horizontally from the LSC plane denote restoring force on the LSC plane due to sidewall pressure. Arrows between diagrams indicate the viewing order to follow the advection of upward- and downward-moving plumes. Slosh displacements are seen at $2\omega_\phi t = 0, \pi$, and twist displacements are seen at $2\omega_\phi t = \pi/2, 3\pi/2$. (*b*) Displacement angles of hot and cold plumes as functions of height and time. They can be seen as travelling waves moving in opposite directions. The $+k$ is for α_h moving to the right with increasing z, and the $-k$ is for α_c moving to the left with increasing z.

a centripetal acceleration, but the calculations can be treated independently and in each case are self-consistent. This means that there are two peaks of the oscillation per cycle of the LSC; the wavenumber is $k = \pi/L$; and the oscillation frequency is $2\omega_\phi$ if the travelling waves are moving at the speed of the LSC. It has been measured that temperature and velocity oscillations have a frequency $U_{max}/2L$, where U_{max} is the maximum of the vertical velocity profile (Qiu & Tong 2001*b*). Particle-image velocimetry measurements have shown that U_{max} overestimates the average LSC speed by about a factor of 1.2, i.e. $U_{max} \approx 1.2\langle U \rangle$ (Sun *et al.* 2005*b*). The path length l of the circulation is given by $l = 3.4L$ for large Ra (Sun & Xia 2005), so the oscillation frequency is $2.0\omega_\phi$, which is self-consistent with the picture of two wavelengths per cycle. Adjusting the path length from the simplification of $4L$ to the measured value of $3.4L$ would require a small adjustment of k but does not shift the frequency. We can now write down the empirical equations of motion. For the oscillating peak positions of the hot upward-travelling waves we have

$$\alpha_h = A\cos(\pi z/L - 2\omega_\phi t), \tag{4.1}$$

and for the cold downward-travelling waves we have

$$\alpha_c = -A\cos(-\pi z/L - 2\omega_\phi t). \tag{4.2}$$

The slosh displacement is

$$\alpha' \equiv \frac{\alpha_h - \alpha_c}{2} = A\cos(\pi z/L)\cos(2\omega_\phi t), \tag{4.3}$$

and the twist displacement is

$$\theta' \equiv \frac{\alpha_h + \alpha_c}{2} = -A\sin(\pi z/L)\sin(2\omega_\phi t). \tag{4.4}$$

This form gives a sloshing oscillation amplitude of $A\cos(\pi z/L)$ which is strongest at the midplane, qualitatively similar to experimental observations (Zhou *et al.* 2009). This gives an amplitude of $A\sin(\pi z/L)$ for the twist which corresponds to $A/\sqrt{2}$ at heights $\pm L/4$ at which the amplitude is measured in experiments. We measured root-mean-square displacement amplitudes $\sigma_{\alpha'} = 0.27$ rad and $\sigma_{\theta'} = 0.18$ rad at $R = 1.1 \times 10^{10}$ (see § 2.2), which yield a ratio of 1.5 in good agreement with the predicted ratio of $\sqrt{2}$.

4.1. *Advected oscillation model*

Since the observed oscillations can be described by a pair of oppositely travelling waves, we now extend the linear oscillation model (3.5) to describe these travelling waves. To describe the torsional oscillation with a stochastic differential equations we must now allow for displacements that vary with height, i.e. a non-planar LSC. With variation in height z the advection term moving along with the LSC is no longer zero as was assumed in earlier versions of the model (Brown & Ahlers 2007*a*). Advection along with the LSC is represented by the term $\dot{\alpha}_a = -u\cdot\nabla\alpha \approx \mp U\,\partial\alpha/\partial z$, where a path length of $4L$ and angular frequency ω_ϕ gives $U = 2\omega_\phi L/\pi$. The advection is upward for the hot plumes and downward for the cold plumes. Taking the time derivative of this term to add it to a second-order equation adds spurious stable solutions with constant $\dot{\alpha} \neq 0$ which we will ignore. Now that α_h and α_c are functions of z, we evaluate the slosh displacement at opposite sides of the sample, i.e. with a phase difference of π. (In part this choice of phase difference is in anticipation of travelling-wave solutions as in (4.7) and (4.8); we could also have chosen to evaluate α_h and α_c at the same height, for example, but that would preclude analytical solutions.) We rewrite (3.5) including this term. Separating equations for α_h and α_c yields

$$\ddot{\alpha}_h(z,t) = -\frac{\dot{\alpha}_h(z,t)}{\tau_{\dot{\theta}}} - \omega_\phi^2\frac{\alpha_h(z,t) - \alpha_c(-z,t)}{2} - \frac{2\omega_\phi L}{\pi}\frac{\partial\dot{\alpha}_h(z,t)}{\partial z} + f_h(z,t) \tag{4.5}$$

and

$$\ddot{\alpha}_c(z,t) = -\frac{\dot{\alpha}_c(z,t)}{\tau_{\dot{\theta}}} - \omega_\phi^2\frac{\alpha_c(z,t) - \alpha_h(-z,t)}{2} + \frac{2\omega_\phi L}{\pi}\frac{\partial\dot{\alpha}_c(z,t)}{\partial z} + f_c(z,t). \tag{4.6}$$

We choose $f_h(z,t)$ and $f_c(z,t)$ so that they have the same Gaussian white noise statistics and magnitude as $f_{\dot{\theta}}(t)$ because they represent the same fluctuations. Possible steady-state solutions of the deterministic parts of (4.5) and (4.6) have the form

$$\alpha_h = A\exp(\mathrm{i}nk_0 z - \mathrm{i}\omega_n t) \tag{4.7}$$

and

$$\alpha_c = A\exp(-\mathrm{i}nk_0 z - \mathrm{i}\omega_n t + \mathrm{i}\psi), \tag{4.8}$$

where $k_0 = \pi/(2L)$. For the circulation to be closed around a loop so that the plume paths are continuous, the solutions must have integer values of n and a relative phase difference $\psi = (n+1)\pi$ between α_h and α_c. Note that because we defined displacements

to be positive if they are counterclockwise from a top view, a positive displacement for upflow followed around the loop becomes a negative displacement for downflow, accounting for the extra phase of π. If we consider the $n=1$ mode with $\psi=0$, there is an in-phase torsional displacement, and an out-of-phase slosh occurs at the top and bottom. These slosh and twist displacements have a relative phase of $\pi/2$. It turns out that the path lengths of the LSC with the out-of-phase slosh displacement and the in-phase twist displacement are exactly the same as for a centred vertical LSC up to second order in α, so there is no restoring force for the $n=1$ mode. The $n=2$ mode corresponds to the observed oscillations of (4.3) and (4.4). There is a restoring force against this slosh displacement for $n=2$ because the path length is shorter than a vertical centred LSC. More generally, the form of the restoring force is complicated and will not give a pure sinusoidal motion. To get a sinusoidal solution as an approximation we calculate the restoring displacement with a phase difference of π. This gives $[\alpha_h(z,t)-\alpha_c(-z,t)]/2=\alpha_h(z,t)[1-\exp(\mathrm{i}\psi)]/2$. This displacement is equal to zero for odd n and equal to $\alpha_h(z)$ for even n. While all even-order modes have some restoring force, the lowest order even mode will dominate because damping will reduce the contributions of higher-order modes. This suggests that the observed mode should be $n=2$ and $k=\pi/L$ in agreement with the empirical equations (4.3) and (4.4).

The solutions have the power spectrum

$$P(\omega)=D_{\dot\theta}\left[\left(\omega^2-\omega_\phi^2-n\omega\omega_\phi\right)^2+(\omega/\tau_{\dot\theta})^2\right]^{-1}. \tag{4.9}$$

In the limiting case of weak damping, the resonant frequency is $\omega_r=(1+\sqrt{2})\omega_\phi$. Resonance with a global maximum in the power spectrum occurs if $1/(\tau_{\dot\theta}\omega_\phi)<2/(1+\sqrt{2})$. Based on independent measurements of the model parameters (Brown & Ahlers 2008*b*) we obtain $1/(\tau_{\dot\theta}\omega_\phi)=2.2$ for $R=1.1\times10^{10}$ which appears to be slightly above the resonance threshold. However, because of the stochastic nature of the damping term $\delta(t)/(\delta_0\tau_\delta)$ of (3.1), the effective damping is much less than the fixed-point value of $1/\tau_{\dot\theta}$ (Brown & Ahlers 2008*a*). Detailed solutions accounting for the variable damping for similar stochastic oscillators have been shown by Gitterman (2005). This effective reduction in damping is very sensitive to the model parameters. It can be as large as an order of magnitude, and it can lead to a large peak at the natural frequency with just a factor-of-two change in one of the parameters. For a system with the same variable-damping term, one can find planar oscillations with a natural frequency weaker by about a factor of five than for the slosh mode (Brown & Ahlers 2008*a*). Since the simple criterion for sustainable oscillations is based on a comparison of the natural frequency with the damping term, the slosh restoring force should easily be strong enough to drive the predicted travelling-wave oscillations. For any value of the damping term that allows resonance, the global resonant frequency remains between $2\omega_\phi$ and $(1+\sqrt{2})\omega_\phi$. So it is within 20 % of the measured frequency of $2.0\omega_\phi$. We see that the model is consistent with the observations if we allow for some uncertainty in the model parameters. However, because a wide range of solutions is possible for this small range of model parameters, the model does not provide a strict test of the oscillation amplitude. A better test comes from the width of the probability distribution in § 3.4.

We fit the predicted background power spectrum (4.9) to the measured power spectrum of α' at the midplane shown in figure 6. We excluded the range $\omega_r/2<\omega<2\omega_r$ and allowed ω_0, $\tau_{\dot\theta}$, n and $D_{\dot\theta}$ to be adjustable parameters. The fit gave $\omega_\phi/(2\pi)=0.0101\pm0.0002$, $\tau_{\dot\theta}=6.1\pm0.1$ s, $n=1.95\pm0.08$ and

$D_{\dot{\theta}} = (1.21 \pm 0.01) \times 10^{-4}$. These fit values of $\tau_{\dot{\theta}}$ and $D_{\dot{\theta}}$ are within 20 % of the parameter values obtained from independent methods based on power spectra of θ_0 (Brown & Ahlers 2008*b*), confirming our assumption that the same values are appropriate to describe the dynamics of α'. The fit value based on the background gives $\omega_\phi = 0.50\omega_r$, where ω_r is the measured peak frequency, which is consistent with our prediction for the $n = 2$ mode in the strong damping limit and with observations. In contrast, for a linear harmonic oscillator the natural frequency is always greater than the resonant frequency. The fact that the fit does not produce a peak is not a concern because (4.9) underestimates the peak as explained in the previous paragraph. The enhancement is all near the natural frequency since $\omega_r \tau_{\dot{\theta}} = 0.9$. The region with a scaling of ω^{-1} is not expected in typical linear harmonic-oscillator equations and appears in the model as a result of the advective term. The crossover to a ω^{-1} scaling with a fit value consistent with $n = 2$ provides support for the advective term in the model.

The probability distributions of angular displacements $p(\alpha')$ and $p(\theta')$ are predicted to be Gaussian (see (3.7)). However, the displacement distribution $p(\alpha')$ at a single height was observed to be flat or even slightly double-peaked as shown by figure 5(*a*). A twist displacement for $n = 2$ has a shorter path length than a centred, planar LSC and thus corresponds to a lower potential. Since this effect is maximized at $\pi/2$ rad out of phase with the slosh displacement, the twist may serve to further drive the oscillation to larger amplitudes, increasing the effective restoring force and giving a flatter or double-peaked probability distribution. An average of the slosh displacements over different heights averages over different phases of the oscillation and thus will tend to give a smoother distribution. The flat probability distribution cannot be seen in the twist because there it is only measured based on a difference in angle at different heights. In any case, the probability distributions based on the height-averaged displacements were shown to be in good agreement with the model. It was observed by Funfschilling *et al.* (2008) that the torsional-oscillation amplitude tends to be larger when the LSC strength δ is weaker. This is expected to be the case both because the restoring and damping frequencies are physically dependent on the LSC strength and because they instantaneously should be proportional to δ, which would tend to widen the probability distribution calculated from (3.7) when δ decreases. A simple substitution does not give an exact result, but we can make a qualitative prediction that the amplitude of oscillations increases as δ decreases.

4.2. *Containers with non-circular cross-sections*

We can apply this model to other geometries by generalizing the diameter function $D(\theta, \alpha')$. This is valid because the potential in (3.4) has the same form as that found for non-circular containers in which the diameter function $D(\theta)$ corresponds to the length of a chord through the centre of a horizontal cross-section as a function of orientation θ (Brown & Ahlers 2008*a*). Since the potential scales as $D(\theta)^{-2}$, the potential minimum corresponds to a longest diameter. In containers with highly elliptical or rectangular cross-sections the sidewall shape was predicted to induce an in-phase torsional oscillation that corresponds to the $n = 1$ mode because the restoring force is proportional to θ_0 measured relative to the longest diameter (Brown & Ahlers 2008*a*). In the interest of studying oscillations in non-circular containers we calculated the generalized diameter function $D(\theta, \alpha')$ for some geometries.

Brown & Ahlers (2008*a*) considered containers with elliptical cross-sections defined by $D(\theta) = L[1 + \varepsilon \cos(2\theta)]$ with ellipticity ε. An elliptical container can be considered a perturbation of a cylindrical container with circular cross-section in which ε is

the small parameter. A second-order expansion around the longest diameter gives $D(\theta, \alpha') = L(1 - 2\varepsilon\theta^2 - \alpha'^2/2)$. The $n = 2$ mode should be dominant for small ε, while the $n = 1$ mode is overdamped, but once ε is large enough that the $n = 1$ mode is underdamped it should soon become dominant because it occurs at lower frequency, so the peak of its power spectrum is reduced least by damping. The restoring forces for the $n = 1$ and $n = 2$ modes are equal for $\varepsilon = 1/4$, so at that point we would expect the $n = 1$ mode to dominate, but because of the complicated effect of fluctuations of δ it is difficult to give a more precise value for a transition.

In a rectangular container of horizontal aspect ratio Λ the potential becomes asymmetric around the diagonal. A first-order expansion around a diagonal gives the diameter function $D_\pm \approx [1 - \Lambda^{\pm 1}(|\theta| + |\alpha'|)]D_m$, where the $\pm$ terms correspond to the two sides of the longest diameter D_m. The scaling with $|\alpha'|$ rather than α'^2 should give a non-sinusoidal oscillation and changes the expected $p(\alpha')$ to a double-sided exponential as explained by Brown & Ahlers (2008*a*) for the in-phase torsional oscillation. The slosh and twist displacements provide equal contributions to the restoring force, so we expect the $n = 1$ mode to dominate in rectangular containers because it is at a lower frequency.

We note that the tilt-induced oscillations studied by Brown & Ahlers (2008*a*) are similar to the predicted cross-section-dependent oscillations because the restoring force is proportional to θ', so this restoring force can drive the $n = 1$ mode. The oscillations found by Brown & Ahlers (2008*a*) had frequencies smaller than ω_ϕ when induced by a small tilt angle and did not have an advective scaling regime in the power spectrum with $P(\omega) \propto \omega^{-1}$. Thus they were best described without the advective term in the model. This can be the case because the restoring force is relative to fixed locations in the container and can perturb the LSC without the requirement of producing closed oscillations. We presume that either type of mode can exist for cross-section-dependent oscillations in which the non-advective mode occurs for small asymmetries with the $n = 1$ advective mode only occurring for larger asymmetries.

5. Conclusions

We used a physically motivated stochastic model to explain the observed torsional and sloshing oscillations. The proposed mechanism for the restoring force is the pressure produced by the sidewall to contain the LSC, which can have a component to drive the LSC towards a shape with a longer path length. This result came from extending an earlier model used to predict that the LSC would align with the longest diameter in a container with non-circular cross-section by simply relaxing the assumption that the LSC travels through the cell centre. By further relaxing the assumption of a planar LSC and adding the necessary advective term which was zero before, this model was extended to describe an advected oscillation which contains both the observed torsional and sloshing modes. Considering pressure gradients due to the sidewalls, advection along the direction of the LSC, inertial damping and a stochastic driving force as the relevant terms, we can explain the structure, frequency and amplitude of the observed oscillations. The apparent torsional and sloshing oscillations can now be understood as manifestations of travelling waves which are advected along with the LSC. Since the restoring force for both oscillation modes comes from the slosh displacement, the out-of-phase torsional mode cannot exist without a sloshing mode.

The agreement of the oscillation frequency with twice the cell-crossing time (Qiu & Tong 2001*b*) was in the past considered as a sign of the alternating emissions of

plumes from the thermal boundary layers (Villermaux 1995). However, it was shown recently that plumes are not emitted alternately from the thermal boundary layers (Xi *et al.* 2009). We have now shown that this agreement can be explained by advection with a natural frequency of the bulk flow. It is notable that we never had to invoke vertical heat transport, thermal boundary layers or spatially or temporally periodic plume emission as either driving forces or boundary conditions. At this point we believe we can explain the origin of all of the known dynamics of the LSC using stochastic differential equations based on approximate volume averages of the Navier–Stokes equations. The physics has included buoyancy, viscous damping, effective damping from rotational inertia, restoring forces from pressure gradients, turbulent fluctuations and various perturbations from asymmetries. Thus the LSC dynamics seem to be inherent to the bulk flow and independent of the thermal boundary layers. The dramatic cessations were described by a different regime of the model in which fluctuations in δ are important, indicating that the two sets of dynamics are independent despite the fact that the duration of a cessation is comparable to an oscillation period. The connection is that these time scales were both fundamentally set by advection.

While we calculated and tested results for cells with circular cross-sections, this model is formulated in such a way that it can be applied to cells with other geometries. Specifically, the diameter function $D(\theta, \alpha')$ describing a horizontal LSC cross-section is used as an input for the model. This can in principle be applied to other container geometries as long as the flow is a single convection roll. Since this model has been so successful at describing the dynamics with a single-roll LSC, the next logical step is to attempt to apply it to more complicated buoyancy-driven convection problems, many of which involve multiple-roll LSCs.

REFERENCES

Ahlers, G., Brown, E. & Nikolaenko, A. 2006 The search for slow transients, and the effect of imperfect vertical alignment, in turbulent Rayleigh–Bénard convection. *J. Fluid Mech.* **557**, 347–367.

Ahlers, G., Grossmann, S. & Lohse, D. 2009 Heat transfer and large scale dynamics in turbulent Rayleigh–Bénard convection. *Rev. Mod. Phys.* **81**, 503–537.

Brown, E. & Ahlers, G. 2006*a* Effect of the Earth's Coriolis force on turbulent Rayleigh–Bénard convection in the laboratory. *Phys. Fluids* **18**, 125108-1–125108-15.

Brown, E. & Ahlers, G. 2006*b* Rotations and cessations of the large-scale circulation in turbulent Rayleigh–Bénard convection. *J. Fluid Mech.* **568**, 351–386.

Brown, E. & Ahlers, G. 2007*a* Large-scale circulation model of turbulent Rayleigh–Bénard convection. *Phys. Rev. Lett.* **98**, 134501-1–134501-4.

Brown, E. & Ahlers, G. 2007*b* Temperature gradients and search for non-Boussinesq effects in the interior of turbulent Rayleigh–Bénard convection. *Europhys. Lett.* **80**, 14001-1–14001-6.

Brown, E. & Ahlers, G. 2008*a* Azimuthal asymmetries of the large-scale circulation in turbulent Rayleigh–Bénard convection. *Phys. Fluids* **20**, 105105-1–105105-15.

Brown, E. & Ahlers, G. 2008*b* A model of diffusion in a potential well for the dynamics of the large-scale circulation in turbulent Rayleigh–Bénard convection. *Phys. Fluids* **20**, 075101-1–075101-16.

Brown, E., Funfschilling, D. & Ahlers, G. 2007 Anomalous Reynolds-number scaling in turbulent Rayleigh–Bénard convection. *J. Stat. Mech.* **2007**, P10005-1–P10005-22.

Brown, E., Nikolaenko, A. & Ahlers, G. 2005 Reorientation of the large-scale circulation in turbulent Rayleigh–Bénard convection. *Phys. Rev. Lett.* **95**, 084503.

Castaing, B., Gunaratne, G., Heslot, F., Kadanoff, L., Libchaber, A., Thomae, S., Wu, X. Z., Zaleski, S. & Zanetti, G. 1989 Scaling of hard thermal turbulence in Rayleigh–Bénard convection. *J. Fluid Mech.* **204**, 1–30.

Ciliberto, S., Cioni, S. & Laroche, C. 1996 Large-scale flow properties of turbulent thermal convection. *Phys. Rev.* E **54**, R5901–R5904.

Cioni, S., Ciliberto, S. & Sommeria, J. 1997 Strongly turbulent Rayleigh–Bénard convection in mercury: comparison with results at moderate Prandtl number. *J. Fluid Mech.* **335**, 111–140.

Funfschilling, D. & Ahlers, G. 2004 Plume motion and large scale circulation in a cylindrical Rayleigh–Bénard cell. *Phys. Rev. Lett.* **92**, 194502.

Funfschilling, D., Brown, E. & Ahlers, G. 2008 Torsional oscillations of the large-scale circulation in turbulent Rayleigh–Bénard convection. *J. Fluid Mech* **607**, 119–139.

Gitterman, M. 2005 *The Noisy Oscillator: The First Hundred Years, from Einstein Until Now*. World Scientific.

Heslot, F., Castaing, B. & Libchaber, A. 1987 Transition to turbulence in helium gas. *Phys. Rev.* A **36**, 5870–5873.

Niemela, J. J., Skrbek, L., Sreenivasan, K. R. & Donnelly, R. J. 2001 The wind in confined thermal turbulence. *J. Fluid Mech.* **449**, 169–178.

Qiu, X. L., Shang, X. D., Tong, P. & Xia, K.-Q. 2004 Velocity oscillations in turbulent Rayleigh–Bénard convection. *Phys. Fluids.* **16**, 412–423.

Qiu, X. L. & Tong, P. 2000 Large-scale coherent rotation and oscillation in turbulent thermal convection. *Phys. Rev.* E **61**, R6075–R6078.

Qiu, X. L. & Tong, P. 2001*a* Large scale velocity structures in turbulent thermal convection. *Phys. Rev.* E **64**, 036304-1–036304-13.

Qiu, X. L. & Tong, P. 2001*b* Onset of coherent oscillations in turbulent Rayleigh–Bénard convection. *Phys. Rev. Lett* **87**, 094501-1–094501-4.

Qiu, X. L. & Tong, P. 2002 Temperature oscillations in turbulent Rayleigh–Bénard convection. *Phys. Rev.* E **66**, 026308-1–026308-12.

Resagk, du Puits, R., Thess, A., Dolzhansky, F.V., Grossmann, S., Fontenele Araujo, F. & Lohse, D. 2006 Oscillations of the large scale wind in turbulent thermal convection. *Phys. Fluids* **18**, 095105-1–095105-15.

Sano, M., Wu, X. Z. & Libchaber, A. 1989 Turbulence in helium-gas free convection. *Phys. Rev.* A **40**, 6421–6430.

Sun, C., Xi, H. D. & Xia, K. Q. 2005*a* Azimuthal symmetry, flow dynamics, and heat transport in turbulent thermal convection in a cylinder with an aspect ratio of 0.5. *Phys. Rev. Lett.* **95**, 074502.

Sun, C. & Xia, K.-Q. 2005 Scaling of the Reynolds number in turbulent thermal convection. *Phys. Rev.* E **72**, 067302-1–067302-4.

Sun, C., Xia, K. Q. & Tong, P. 2005*b* Three-dimensional flow structures and dynamics of turbulent thermal convection in a cylindrical cell. *Phys. Rev.* E **72**, 026302-1–026302-13.

Takeshita, T., Segawa, T., Glazier, J. A. & Sano, M. 1996 Thermal turbulence in mercury. *Phys. Rev. Lett.* **76**, 1465–1468.

Tsuji, Y., Mizuno, T., Mashiko, T. & Sano, M. 2005 Mean wind in convective turbulence of mercury. *Phys. Rev. Lett.* **94**, 034501.

Villermaux, E. 1995 Memory-induced low frequency oscillations in closed convection boxes. *Phys. Rev. Lett.* **75**, 4618–4621.

Xi, H. D., Zhou, Q. & Xia, K. Q. 2006 Azimuthal motion of the mean wind in turbulent thermal convestion. *Phys. Rev.* E **73**, 056312-1–056312-13.

Xi, H.-D., Zhou, S.-Q., Zhou, Q., Chan, T.-S. & Xia, K.-Q. 2009 Origin of the temperature oscillation in turbulent thermal convection. *Phys. Rev. Lett.* **102**, 044503.

Zhou, Q., Xi, H.-D., Zhou, S.-Q., Sun, C. & Xia, K.-Q. 2009 Oscillations of the large-scale circulation in turbulent Rayleigh–Bénard convection: the sloshing mode and its relationship with the torsional mode. *J. Fluid Mech.* **630**, 367–390.